Chinese Chemical Letters 37 (2026) 112129

Contents lists available at ScienceDirect

Chinese Chemical Letters

journal homepage: www.elsevier.com/locate/cclet

Synergistic antitumor therapy *via* immunophototherapy induced multi-modal cell death and immune microenvironment reprogramming

Xinyu Wang[a], Yunquan Yang[a], Shaojing Zhao[b], Yuanyu Tang[b], E Pang[b], Wenjie Gao[c], Jiwei Li[d], Qingxu Diao[e], Lianhong Zou[e,*], Jie Zeng[f,*], Minhuan Lan[b,*], Jianing Yi[e,f,*]

[a] *Department of General Surgery, The Affiliated Changsha Hospital of Xiangya School of Medicine, Central South University, Changsha 410005, China*
[b] *College of Chemistry and Chemical Engineering, Central South University, Changsha 410083, China*
[c] *Department of General Surgery, Sir Run Run Hospital of Nanjing Medical University, Nanjing 211166, China*
[d] *Department of Oncology, The Second Xiangya Hospital, Central South University, Changsha 410000, China*
[e] *Institute of Clinical and Translational Medicine, Hunan Provincial People's Hospital, The First Affiliated Hospital of Hunan Normal University, Changsha 410005, China*
[f] *Department of Breast and Thyroid Gland Surgery, Hunan Provincial People's Hospital, The First Affiliated Hospital of Hunan Normal University, Changsha 410005, China*

ARTICLE INFO

Article history:
Received 20 July 2025
Revised 16 November 2025
Accepted 17 November 2025
Available online 17 November 2025

Keywords:
Aggregate
Near infrared
Immuno-phototherapy
Immunogenic cell death
PANoptosis

ABSTRACT

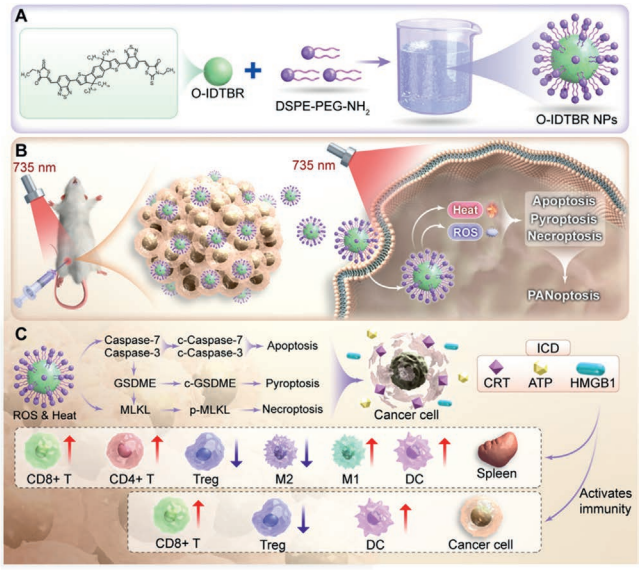
This study aims to develop advanced phototheranostic agent to address the critical challenge of multi-modal therapy and immune microenvironment remodeling in immuno-phototherapy (IPT). Here we utilized a near infrared (NIR) *o*-IDTBR, and then assembled with 1,2-distearoyl-*sn*-glycero-3-phosphoethanolamine-*N*-[amino(polyethylene glycol)] (DSPE-PEG-NH_2) to prepare *o*-IDTBR nanoparticles (NPs). Theoretical calculations suggest that in the aggregated state, the energy gap between the highest occupied molecular orbital (HOMO) and lowest unoccupied molecular orbital (LUMO), and the energy gap between the excited singlet and triplet states are reduced, as compared to the monomolecular state, leading to red-shifting absorption/emission wavelengths and enhancing the photothermal conversion and reactive oxygen species (ROS) generation, and thus improve the efficacy of photodynamic and photothermal therapies. These NIR laser-activated NPs effectively induced pyroptosis/apoptosis/necroptosis (PANoptosis) and promoted immunogenic cell death through mechanisms such as calreticulin (CRT) exposure, ATP secretion, and high mobility group box 1 (HMGB1) release. Notably, immune profiling revealed a reprogrammed tumor microenvironment in NPs and laser irradiation treated group. This phenotypic shift activated systemic antitumor immunity. Our work constructs an advanced phototheranostic agent with aggregation-induced red-shifting absorption and fluorescence wavelengths, and enhancing photothermal conversion and ROS generation capabilities, and establishes a synergistic paradigm of "imaging guidance, inducing local multi-modal cell death, systemic immune activation".

© 2026 Published by Elsevier B.V. on behalf of Chinese Chemical Society and Institute of Materia Medica, Chinese Academy of Medical Sciences.

Immuno-photodynamic therapy (IPDT), an innovative tumor treatment strategy, combines photodynamic therapy (PDT) with immune modulation to achieve multidimensional intervention against malignancies [1–3]. Its mechanism operates on two levels: Photophysically, photosensitizers activated by specific light wavelengths generate singlet oxygen ($^1O_2$) *via* energy transfer [4], triggering localized tumor apoptosis; Immunologically, programmed cell death releases damage-associated molecular patterns (DAMPs) and tumor-specific antigens, initiating systemic antitumor immunity to target metastatic lesions [5]. Compared to conventional PDT, IPDT retains advantages such as precise targeting, minimal drug resistance, and controllable toxicity while offering three clinical breakthroughs: Dose optimization reduces systemic toxicity and broadens the therapeutic window; Immune-stimulating factors remodel the immunosuppressive tumor microenvironment (TME), enhancing effector T cell and antigen-presenting cell infiltration; Long-term immune memory formation inhibits tumor recurrence

* Corresponding authors.
E-mail addresses: yijianing@hunnu.edu.cn (J. Yi), minhuanlan@csu.edu.cn (M. Lan), zengjie227@hunnu.edu.cn (J. Zeng), zoulh1986@hunnu.edu.cn (L. Zou).

https://doi.org/10.1016/j.cclet.2025.112129
1001-8417/© 2026 Published by Elsevier B.V. on behalf of Chinese Chemical Society and Institute of Materia Medica, Chinese Academy of Medical Sciences.



Scheme 1. (A) A schematic diagram illustrating the preparation of *o*-IDTBR NPs to 735 nm laser irradiation, leading to tumor cell death *via* PANoptosis (B). (C) The combined effects of PDT and PTT promote multi-modal cell death pathways in tumor cells and the formation of *in situ* tumor vaccines.

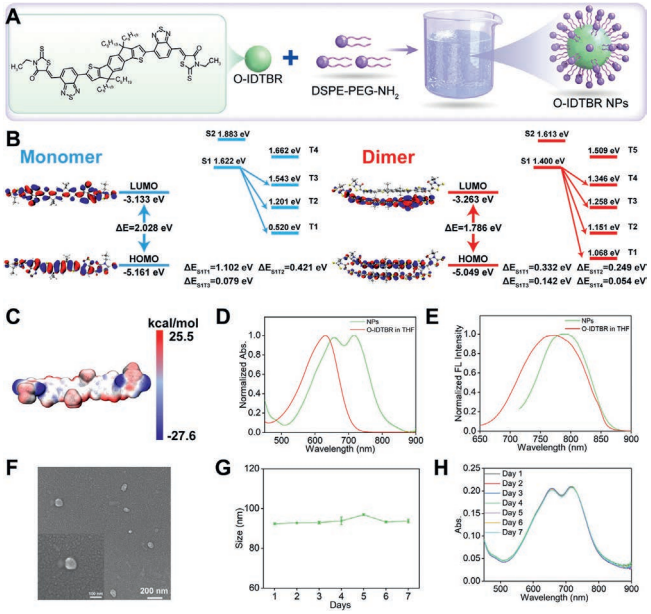


Fig. 1. (A) Schematic representation illustrating the preparation of NPs. (B) Diagram showing the calculated frontier molecular orbitals of monomeric and dimeric NPs, alongside the energy levels of the singlet and triplet excited states for both monomeric and dimeric forms. (C) ESP map of *o*-IDTBR. (D) Absorption and (E) fluorescence spectra of NPs in aqueous solution compared to *o*-IDTBR in THF. (F) SEM image of NPs. Time-dependent changes in (G) particle distribution and (H) absorption spectra of NPs.

[6,7]. This spatiotemporal synergy not only amplifies local tumor ablation but also achieves a paradigm shift from localized treatment to systemic immune defense [8,9].

However, the efficacy of IPDT is hindered by the hypoxic TME [10–12]. Oxygen dependency limits $^1O_2$ generation during PDT, while hypoxia-driven hypoxia-inducible factor 1-alpha (HIF-1α) activation promotes metabolic reprogramming (*e.g.*, enhanced glycolysis) and immune cell exhaustion (*e.g.*, suppressed cytotoxic T lymphocytes and expanded myeloid-derived suppressor cells) [13,14]. Furthermore, immunosuppressive networks formed by M2 macrophages and regulatory T cells (Tregs) *via* inhibitory cytokines like interleukin-10 (IL-10) further dampen antitumor immunity [15]. Current strategies to mitigate hypoxia only partially address these limitations. Moreover, traditional immunogenic cell death (ICD) mechanisms in IPDT often fail to release sufficient tumor antigens or elicit robust cross-presentation, resulting in suboptimal *in situ* vaccination [16,17]. Additionally, homogeneous immune cell changes induced by single-mode ICD impair immune memory formation [18,19]. These challenges necessitate interdisciplinary solutions to enhance systemic immune activation.

Recent studies highlight the immunostimulatory potential of photothermal-photodynamic (PTT-PDT) synergy [20–22]. Photothermal-mediated vasodilation improves tissue oxygenation and overcomes oxygen dependence of PDT [23–25]. Developing single-near infrared (NIR)-wavelength activated phototheranostic agents capable of effectively generating $^1O_2$ generation and conversing photon energy into heat is thus pivotal for advancing cancer therapy [26].

o-IDTBR consists of an electron-donating ladder-type fused five-member-ring indaceno[1,2-b:5,6-*b*′]dithiophene (IDT) core with aliphatic *n*-octyl side chains flanked by two electron withdrawing benzothiadiazole moieties and rhodanine terminated groups (Scheme 1A). The four alkyl substituents ensure solubility for solution processing and appropriate aggregation after forming water-dispersible nanoparticles (NPs) by assembling with 1,2-distearoyl-*sn*-glycero-3-phosphoethanolamine-*N*-[amino(polyethylene glycol)] (DSPE-PEG-NH2). The amphiphilic polymer DSPE-PEG-NH_2 was chosen to encapsulate *o*-IDTBR *via* nanoprecipitation. Its hydrophobic DSPE segment anchors into the hydrophobic core of the NP, while the hydrophilic PEG chain forms a hydrated shell that confers excellent colloidal stability, stealth properties to reduce opsonization, and biocompatibility. The terminal amine group (-NH_2) also provides potential for future surface functionalization. Interestingly, after formation NPs, the energy gap between the highest occupied molecular orbital (HOMO) and lowest unoccupied molecular orbital (LUMO) (ΔE), and the ΔE_{ST} are reduced, which is not only favorable to red-shift the wavelengths of absorption and fluorescence emission, but also enhance the ability to convert photon energy into heat and reactive oxygen species (ROS).

The *o*-IDTBR NPs developed in this study demonstrates remarkable multifunctional theranostic properties. As illustrated in Scheme 1B, under 735 nm laser irradiation, tumor cells co-cultured with *o*-IDTBR NPs were effectively eradicated through multi-modal cell death mechanisms, including ICD and pyroptosis/apoptosis/necroptosis (PANoptosis) induced by the combined action of PTT and PDT. Mechanistic studies reveal that NIR laser-activated *o*-IDTBR NPs exert synergistic therapeutic effects through multi-modal cell death pathways Furthermore, it promotes the production of *in situ* tumor vaccine and improves the residence of immune memory cells (Scheme 1C). These effects collectively reshape the immune microenvironment, thereby improving the efficacy of immuno-phototherapy against tumors. This work establishes a paradigm for developing next-generation integrated phototoimmunotherapy platforms.

According to Fig. 1A, this A-A'-D-A'-A structure with strong intramolecular charge transfer (ICT) endows *o*-IDTBR with significant NIR fluorescence/absorption properties. Meanwhile, the alkyl substituents ensure the solubility for solution processing and appropriate aggregation after forming NPs by assembling with DSPE-PEG-NH_2. As shown in Fig. 1B (left: monomer), the ΔE between HOMO and LUMO was 2.028 eV, giving it a NIR emission. Moreover, the electrostatic potential (ESP) map of NPs in Fig. 1C indicates that positive charges are concentrated on the indaceno[1,2-*b*:5,6-*b*′]dithiophene (IDT) core, whereas negative charges are pre-

dominantly located on the benzothiadiazole moieties and rhodanine terminated groups units. The above results imply the strong ICT effect in NPs. Furthermore, the ΔE_{ST} was very small, with a small ΔE_{S1T3} of 0.079 eV was calculated, enhancing the intersystem crossing (ISC) and generation of $^1O_2$.

Next, the ΔE_{ST} of the *o*-IDTBR dimer was further calculated in order to predict the photophysical properties in the aggregate states. Fig. 1B (right dimer) shows that the HOMO is primarily localized on both molecules, whereas the LUMO is predominantly on one molecule, facilitating strong ICT and enhancing photothermal conversion efficiency (PCE). While the monomeric state exhibits only ICT, the aggregated state benefits from additional ICT. This synergistic effect leads to a reduction in both ΔE and ΔE_{ST}, which is responsible for the observed red-shifted absorption/emission and the simultaneous enhancement of photothermal and photodynamic efficiencies.

The photophysical properties of *o*-IDTBR were systematically characterized. As shown in Figs. 1D and E, the *o*-IDTBR dissolved in tetrahydrofuran (THF) solvent exhibited NIR absorption peaks at 630 nm, and fluorescence peak at 771 nm, respectively. Notably, after molecular self-assembly with the amphiphilic block copolymer DSPE-PEG-NH_2, the resulting NPs displayed significant spectral red shifts and broaden: The absorption peak shifted to 720 nm, and the fluorescence emission peak migrated to 793 nm. This wavelength shift originates from the strong intermolecular π-π stacking during NP formation. Morphological analysis by scanning electron microscopy (SEM) (Fig. 1F) revealed that the NPs are spherical and monodisperse. This observation is corroborated by dynamic light scattering (DLS) data (Fig. S1 in Supporting information), which shows an average hydrodynamic diameter of 114 nm with a polydispersity index (PDI) of 0.471, confirming the formation of monodisperse spherical NPs. The ζ-potential is −13.7 mV, enabling the excellent water dispersibility and stability. The moderate negative surface charge enhances cellular uptake efficiency through electroosmotic effects. Furthermore, the particle distribution and absorption spectra of NPs remained stable over seven days (Figs. 1G and H).

The *o*-IDTBR NPs also exhibited outstanding photostability. As shown in Figs. 2A–C, under continuous 735 nm laser irradiation, the absorption spectra of NPs showed negligible changes after 10 min of exposure, whereas the clinical control indocyanine green (ICG) displayed significant spectral attenuation under identical conditions. Further cyclic stability tests (Fig. 2D) demonstrated robust photothermal cycling performance of NPs over five laser on/off cycles (10 min irradiation/10 min cooling). Notably, during the fifth irradiation cycle, the solution temperature reached to ~50 °C, compared to only 41 °C for ICG under the same condition, validating the superior photodegradation resistance of the NPs. Systematic evaluation of photothermal conversion performance (Fig. 2E) revealed a dual concentration- and time-dependent temperature rise in NPs. For instance, 12.5 μmol/L NPs in aqueous solution reached to ~50 °C after 10 min of 735 nm laser irradiation (1 W/cm^2), while pure water showed a mere 3 °C increase. Remarkably, the calculated PCE at 12.5 μmol/L is 44.2 % (Fig. 2F), underscoring the exceptional capability of NPs to convert photon energy into heat.

We further investigated the ROS generation capability and photodynamic therapeutic potential of NPs. As shown in Figs. 2G–L, when aqueous solutions of NPs were exposed to laser irradiation, a significant decrease in absorbance of the $^1O_2$ probe (ABDA) was observed, confirming $^1O_2$ production. Concurrently, a marked increase in fluorescence intensity of the $O_2^{\bullet-}$ probe (DHR123) validated the efficient generation of $O_2^{\bullet-}$. In contrast, no notable changes in ABDA absorbance or DHR123 fluorescence were detected in the absence of NPs. These findings underscore the robust ability of NPs to produce both $^1O_2$ and $O_2^{\bullet-}$ upon 735 nm laser activation, a critical feature for effective PDT. Furthermore, the calculated singlet oxygen quantum yield ($\Phi\Delta$) is 20.3 %. The *o*-IDTBR NPs in aqueous solution exhibited robust generation of both $^1O_2$ and $O_2^{\bullet-}$. In stark contrast, *o*-IDTBR in THF generated only a negligible amount of $^1O_2$ and virtually no detectable $O_2^{\bullet-}$ under identical laser irradiation conditions (Figs. S2A and B in Supporting information). This dramatic difference in ROS generation efficiency between the aggregated state (NPs) and the monomolecular state (THF solution) aligns perfectly with our theoretical calculations, which predicted a reduced ΔE_{ST} in the aggregate that would facilitate more efficient ISC.

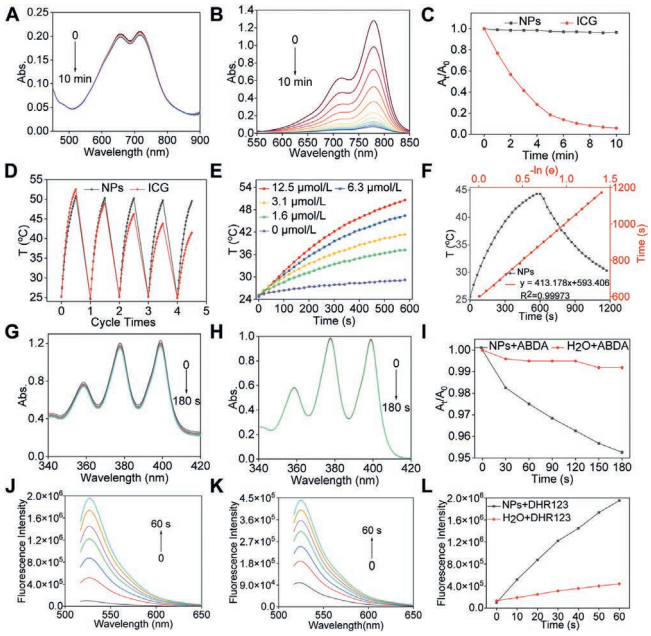


Fig. 2. The changes in the absorption spectra of (A) NPs and (B) ICG under 735 nm laser irradiation (0.5 W/cm^2) for 10 min. (C) Time-dependent variations of absorbance at 720 nm for NPs and at 779 nm for ICG. (D) Temperature variations of NPs and ICG subjected to 735 nm laser at 1 W/cm^2 over 5 cycles. (E) Time-dependent temperature changes of NPs at varying concentrations following laser irradiation. (F) PCE of NPs. Absorption spectral changes of ABDA were observed both with (G) and without (H) 5 μmol/L NPs following exposure to irradiation of 735 nm laser. (I) Changes in the corresponding absorbance ratio (A_t/A_0) at 378 nm of ABDA. Fluorescence spectra changes of DHR123 in (J) the presence and (K) the absence of 5 μmol/L NPs after being exposed to 735 nm laser irradiation. (L) Changes in the corresponding fluorescence intensity at 529 nm of DHR123.

As shown in Fig. S4 (Supporting information), 4T1 cells effectively internalized *o*-IDTBR NPs, exhibiting distinct red fluorescence. To further investigate the endocytic mechanisms, cells were pretreated with various inhibitors or subjected to low-temperature conditions. Fig. S4 demonstrates that the red fluorescence was abolished in cells treated with amiloride or under low-temperature incubation, indicating that cellular uptake of the NPs occurs primarily through macropinocytosis and endocytosis. Subcellular localization studies revealed that *o*-IDTBR NPs predominantly accumulated (Figs. 3A and B).

To further investigate intracellular ROS generation, laser confocal microscopy was employed (Fig. 3C, Figs. S5 and S6 in Supporting information). Strong green fluorescence ($^1O_2$) and red fluorescence ($O_2^{\bullet-}$) were observed in 4T1 cells treated with 25 μmol/L NPs and exposed to 735 nm laser irradiation. These fluorescence signals confirmed robust intracellular production of $^1O_2$ and $O_2^{\bullet-}$. In contrast, no significant fluorescence was detected in cells untreated with NPs or unexposed to laser irradiation, further validating NPs ability to efficiently enter cells and generate ROS under laser activation. Cytotoxicity assays revealed the system's pre-

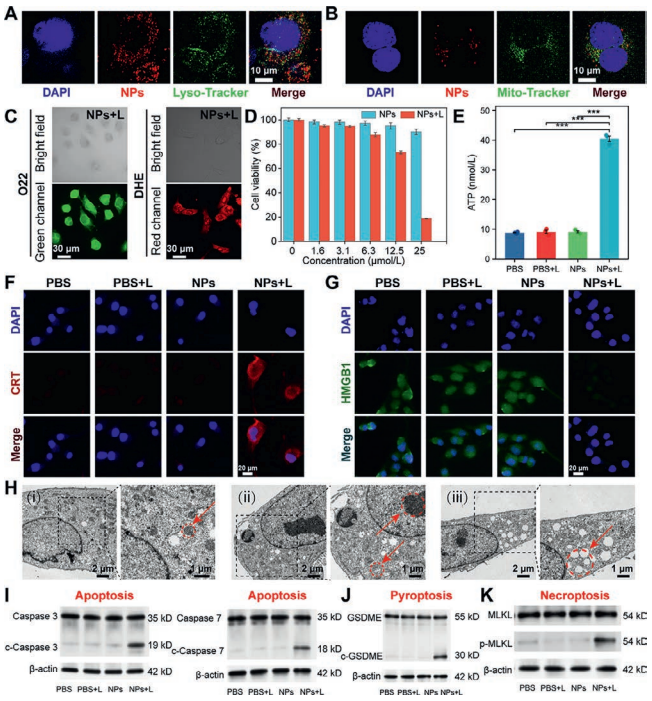


Fig. 3. Enrichment of *o*-IDTBR NPs with lysosomes (A) and mitochondria (B) in 4T1 cells. (C) $^1O_2$ and $O_2^{\bullet-}$ production of tumor cells after treatment. (D) Cell viability and (E) extracellular ATP of tumor cells exposed to NPs, with or without laser. Fluorescent images of (F) CRT exposure and (G) HMGB1 release in tumor cells. (H) The different types of death in 4T1 cells observed by bio-TEM. (I) Western blot analysis of c-caspase 3/7, (J) c-GSDME, and (K) p-MLKL expression in tumor cells after different treatments. The data are shown as the mean ± standard deviation (SD) (D: $n = 12$, E: $n = 3$), as calculated using one-way ANOVA with $^{***}P < 0.001$. DAPI, 4′,6-diamidino-2-phenylindole.

cise light-controlled therapeutic properties (Fig. 3D). Cells incubated with 25 μmol/L NPs in the dark exhibited over 90 % viability, demonstrating excellent biocompatibility. However, upon laser activation (1 W/cm^2), cell viability plummeted to approximately 18 %, indicating extensive cell death. This reduction in survival was concentration-dependent, with higher NP concentrations leading to more pronounced cytotoxicity post-irradiation. Given that tumor hypoxia represents a major challenge for photodynamic therapy, we further evaluated the therapeutic efficacy under hypoxic conditions. As illustrated in Fig. S7 (Supporting information), the combined treatment of 25 μmol/L NPs with laser irradiation achieved a 60 % eradication rate of 4T1 cells even under hypoxia, compared to an 82 % eradication rate under normoxic conditions. This maintained efficacy is attributed to the combined Type II PDT and PTT effects generated by *o*-IDTBR NPs + L. These results underscore the potent phototoxicity of NPs, positioning them as promising candidates for light-triggered phototherapeutic applications.

The synergistic PDT and PTT mediated by NPs induce ICD, characterized by the release of DAMPs. Under 735 nm laser activation, NPs trigger the release of a triad of DAMPs from tumor cells: Calreticulin (CRT) exposure, ATP secretion, and high mobility group box 1 (HMGB1) release. As shown in Fig. 3E, extracellular ATP levels in 4T1 cells treated with NPs and laser irradiation were significantly higher than in cells treated with NPs, confirming that the combination effectively induces ATP release-a hallmark of ICD. Furthermore, strong red fluorescence indicative of CRT exposure on the cell surface was observed in the treated tumor cells (Fig. 3F). In contrast, no significant CRT exposure was detected in cells treated with NPs, highlighting the critical role of laser activation in initiating this process. Immunofluorescence using an HMGB1-specific antibody further validated HMGB1 release (Fig. 3G). Bright green fluorescence, indicating intracellular retention of HMGB1, was observed in cells treated with phosphate-buffered saline (PBS), PBS + laser (L), or NPs. However, in cells treated with laser irradiation and NPs, the absence of fluorescence confirmed HMGB1 release, further corroborating ICD induction. We have performed additional experiments to track the kinetics of CRT exposure, HMGB1 release and ATP secretion over time (1, 3, 6, 12, 24 h post-irradiation). CRT exposure secretion peaks around 3 h, while HMGB1 release becomes significant after 3 h and is nearly complete by 6 h (Figs. S8A and B in Supporting information). For extracellular ATP, we observed a sharp, transient peak within 10 min after laser irradiation. This is consistent with the well-documented short half-life of extracellular ATP, which is rapidly hydrolyzed by ectonucleotidases present in the microenvironment. Therefore, measuring ATP at this early time point is crucial and biologically most relevant, while levels diminished significantly by 1 h (Fig. S9 in Supporting information). Collectively, these findings demonstrate that NPs combined with laser irradiation robustly promote CRT surface exposure and stimulate ATP and HMGB1 release. This process enhances tumor cell immunogenicity, facilitating dendritic cells (DCs)-mediated recognition and phagocytosis, thereby activating a potent antitumor immune response. These results underscore the potential of NPs as an effective strategy for enhancing cancer immunotherapy through targeted ICD induction.

The *o*-IDTBR nanosystem triggers a cascade of multi-modal programmed cell death (PANoptosis) through photoactivation, involving apoptosis, pyroptosis, and necroptosis. This process is coordinated by the formation of the PANoptosome complex, a molecular hub that drives the activation of these distinct yet interconnected cell death pathways [27,28]. To evaluate the induction of PANoptosis by NPs under laser irradiation, we analyzed ultrastructural changes in cell death using biological transmission electron microscopy (bio-TEM). As shown in Fig. 3H(i), untreated cancer cells exhibited normal morphology with intact organelles such as mitochondria. Following treatment with NPs + L, Fig. 3H(ii) revealed characteristic apoptotic features including chromatin condensation, necroptotic processes evidenced by mitochondrial damage, and pyroptotic morphology marked by membrane bubbling (Fig. 3H(iii)). In parallel, key markers of apoptosis, pyroptosis, and necroptosis were analyzed. As shown in Figs. 3I–K, c-caspase 3/7 (apoptosis markers), c-GSDME (pyroptosis markers), and p-MLKL (necroptosis markers) were significantly upregulated in tumor cells treated with NPs and subjected to laser irradiation. The presence of these markers provides strong evidence that NPs, in combination with laser irradiation, trigger the activation of all multi-modal cell death. This phenomenon amplifies the immunogenic therapeutic effects, facilitating the release of DAMPs such as CRT, HMGB1, and ATP. These DAMPs are critical for eliciting ICD, thereby enhancing antitumor immune responses.

In summary, the combination of NPs with laser irradiation not only induces PANoptosis in cancer cells but also amplifies the ICD effect, positioning this strategy as a promising approach for cancer immunotherapy. This multi-modal therapy offers two critical advantages: It simultaneously targets tumor cells through multi-modal cell death mechanisms and activates the immune system to mount robust antitumor responses.

Fig. 4A illustrates the *in vivo* anti-tumor therapy treatment scheme. The animal experiments were approved by the Ethics Committee for Experimental Animals of the First Affiliated Hospital of Hunan Normal University. As shown in Fig. 4B, NIR fluorescence signals were observed at the tumor site following intratumoral injection of NPs, enabling real-time tumor imaging for monitoring tumor localization and therapeutic progression. This capability is particularly valuable for guiding subsequent treatments such as PTT or PDT. Infrared thermal imaging further demonstrated the precision of photothermal efficacy (Fig. 4C). Exposure to 735 nm

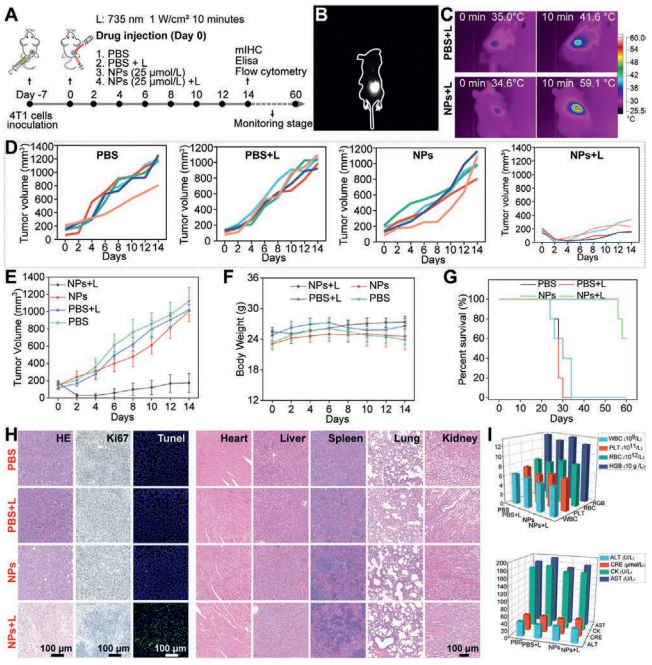


Fig. 4. (A) *In vivo* antitumor therapy treatment schedule. (B) NIR fluorescence images and (C) photothermal images of tumor. Time-dependent variations in (D, E) tumor volume and (F) body weight of mice in the various groups. (G) Survival rates following different treatments. (H) Histological analysis of tumors *via* H&E, Ki67, and TUNEL staining for apoptosis, and H&E staining of major organs from mice. Scale bar: 100 μm. (I) Blood biochemistry and routine analysis. Data are presented as mean ± SD (D–G: $n = 5$; I: $n = 3$).

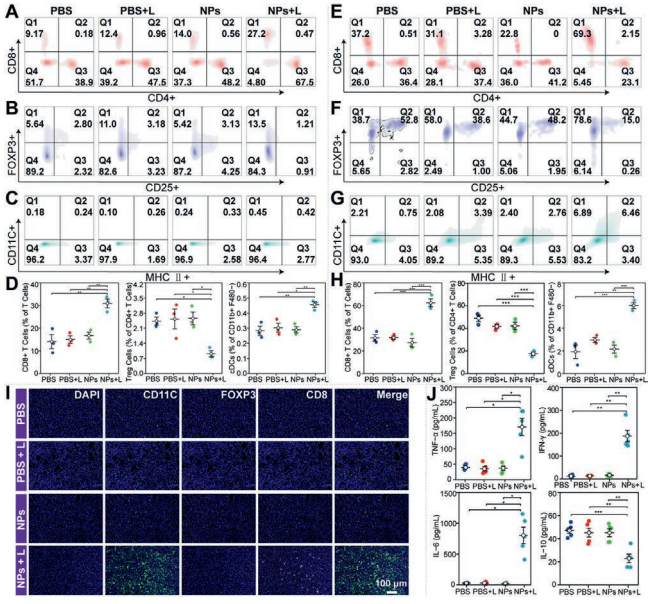


Fig. 5. Comparison of the immune microenvironment of mice (A–D) spleen and (E–H) tumor following different treatments. (I) Multiplex immunohistochemical analysis of tumor sections. (J) Cytokine analysis of serum. The data are shown as the mean ± SD ($n = 3$), as calculated using one-way ANOVA with $^{*}P < 0.05$, $^{**}P < 0.01$, $^{***}P < 0.001$.

laser irradiation, the temperature at the tumor site reached 59.1 °C. In contrast, tumors without NPs exhibited a much smaller temperature increase, reaching only 41.6 °C under identical irradiation conditions. This marked difference confirms the superior *in vivo* photothermal responsiveness of NPs, which can be leveraged for targeted tumor thermal ablation. These results validate the dual functionality of NPs *in vivo*: They serve not only as effective agents for NIR fluorescence imaging but also exhibit exceptional photothermal properties. The study successfully establishes a closed-loop theranostic system encompassing "imaging guidance-thermal therapy implementation-efficacy evaluation", advancing the development of personalized immuno-phototherapy.

The *in vivo* phototherapeutic efficacy of NPs was further investigated. As shown in Figs. 4D and E, in a 4T1 tumor-bearing murine model, the NPs combined with laser irradiation demonstrated significant tumor growth inhibition compared to the PBS, PBS+L, and NPs groups. Notably, no significant differences in body weight were found among the four groups (Fig. 4F), suggesting minimal systemic toxicity and underscoring the safety of this approach. Moreover, the survival rate in NPs+L group was significantly higher than that in other groups (Fig. 4G). Histopathological analyses elucidated three dimensions of the therapeutic mechanism (Fig. 4H): Hematoxylin and eosin staining (H&E) staining identified extensive necrotic regions in the NPs+L group tumor, indicative of substantial tissue damage and tumor cell death following combination therapy. Ki67 marker analysis demonstrated effective suppression of cellular proliferation in the NPs+L group. In the same group, enhanced apoptosis was confirmed by terminal deoxynucleotidyl transferase dUTP nick-end labeling (TUNEL) staining. These findings collectively demonstrate that NPs with laser irradiation can inhibit tumor cell proliferation, and promote tumor cell necrosis and apoptosis. The clinical safety profile of NPs was rigorously validated through a comprehensive toxicological evaluation. Histopathological analysis (Fig. 4H) of major organs (liver, kidney, heart, and spleen) from mice treated with NPs or in combination with laser irradiation revealed no significant tissue damage, inflammation, or adverse effects in any organ, as evidenced by H&E staining. These findings strongly indicate that intratumoral injection of NPs is biocompatible and safe, with no acute toxicity or organ dysfunction. Further safety assessments *via* blood routine tests and biochemical analyses (Fig. 4I) focused on hematological parameters and the functionality of critical organs. Results showed no significant deviations in key indicators, including red blood cell (RBC), white blood cell (WBC), platelets, aspartate aminotransferase (AST), alanine aminotransferase (ALT), creatinine, blood urea nitrogen (BUN), and cardiac biomarkers, confirming the absence of systemic toxicity.

The immunomodulatory network mediated by NPs under laser irradiation was systematically evaluated using flow cytometry and multiplex immunohistochemistry of tissue sections. As shown in Figs. 5A–D and Fig. S10 (Supporting information), quantitative flow cytometric analysis revealed that NPs combined with laser irradiation (NPs+L group) significantly increased the infiltration of $CD4^+$ and $CD8^+$ T cells in the spleen compared to control groups (PBS, PBS+L, and NPs). Enhanced infiltration of $CD4^+/CD8^+$ T cells indicates that NPs+L therapy effectively stimulates adaptive immune responses mediated by these cells, which are critical for triggering tumor-specific immunity and promoting tumor rejection. Furthermore, NPs+L treatment markedly elevated the number of mature DCs, essential for antigen presentation and T cell activation. Notably, the proportion of M1 macrophages (associated with antitumor activity) increased, while immunosuppressive cell populations, including Treg cells and M2 macrophages, were reduced. Further analysis *via* immunofluorescence staining of tumor tissues revealed an increase in both $CD8^+$ T cells and DCs within the tumor, as shown in Figs. 5E–I. These observations reinforce the idea that DCs are activated upon antigen recognition and migrate to the lymph nodes, where they present the tumor-associated antigens to T cells, further amplifying the cell-mediated immune response against the tumor. The immune activation induced by NPs + L treatment was further confirmed by analyzing the levels of key pro-inflammatory and regulatory cytokines in serum. Cytokine profile analysis

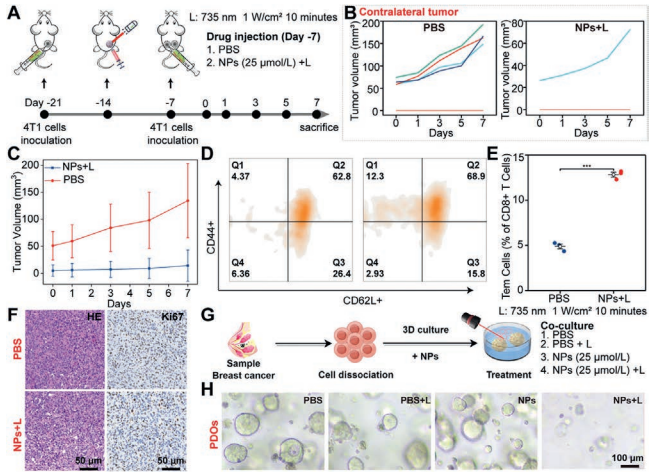


Fig. 6. (A) Treatment scheme of antitumor therapy with immune memory *in vivo*. (B, C) Time-dependent changes in tumor volume of mice in the various groups. (D, E) Comparison of the immune microenvironment of mice spleen following different treatments. (F) Histological analysis of tumors *via* H&E and Ki67 staining. (G) Treatment scheme of organoids. (H) Bright images of organoids. The data are shown as the mean ± SD (B, C: $n = 5$; D, E: $n = 3$), as calculated using one-way ANOVA with $^{***}P < 0.001$.

(Fig. 5J) further validated immune activation induced by NPs+L therapy. Levels of proinflammatory cytokines tumor necrosis factor-alpha (TNF-α) and interferon-γ (IFN-γ), critical for T cell activation and tumor suppression, were significantly elevated in both tumor and spleen tissues. Conversely, levels of immunosuppressive cytokines IL-6 and IL-10 were reduced. These results indicate that the treatment not only activates robust immune responses but also counteracts immunosuppressive signaling within the TME, synergistically enhancing antitumor immunity.

Fig. 6A illustrates the experimental design for evaluating *in vivo* immunomemory-mediated antitumor therapy. As shown in Figs. 6B and C, 80% (4/5) of PBS-treated mice developed distant tumors, whereas only 20% (1/5) of mice in the NPs+L group developed tumors, with significantly smaller tumor volumes compared to the PBS group. To validate the immunomemory effect induced by NPs+L therapy, splenocytes from both groups were quantitatively analyzed *via* flow cytometry (Figs. 6D and E). The NPs+L group exhibited a substantially increased proportion of effector memory T cells (Tem cells) in the spleen compared to the PBS group, confirming the establishment of adaptive immunomemory critical for tumor rejection, prevention of metastasis and recurrence. Comparative analysis of tumor sections (Fig. 6F) revealed similar histoarchitectural features between groups by H&E staining. However, Ki67 proliferation marker assessment demonstrated reduced tumor cell proliferation in the NPs+L group. These results collectively indicate that the combination therapy induces systemic immunomemory, effectively inhibiting contralateral tumor cell division and growth while promoting tumor rejection and preventing metastasis and recurrence.

At the translational level, efficacy validation using patient-derived organoids (PDOs) from solid tumors (Figs. 6G and H) demonstrated that NPs combined with laser irradiation significantly suppressed tumor growth, underscoring their potent antitumor activity. These comprehensive evaluations conclusively establish that NPs, when combined with laser irradiation, not only deliver effective antitumor therapy but also exhibit excellent biocompatibility with minimal systemic toxicity. By constructing a progressive evaluation framework spanning experimental animals to humanized models, this study lays a robust toxicological foundation for the clinical translation of NPs.

This study successfully developed a novel immunophototherapeutic agent, whose innovation lies in the synergistic integration of inducing multi-modal cell death and immune modulation. As compared with the monomolecular state, these NPs exhibit aggregation-induced red-shifting absorption and fluorescence emission wavelengths, and aggregation-induced enhanced photothermal conversion and ROS generation capabilities, providing a precise tool for real-time imaging guidance phototherapy of deep-seated tumors. This overcomes the long-standing technical limitation of conventional photosensitizers in balancing photothermal and oxidative stress effects. Furthermore, PDT and PTT synergistically induced PANoptosis and ICD in tumor cells, as evidenced by enhanced infiltration of $CD4^+$ and $CD8^+$ T cells, M1 macrophage polarization, and reduced proportions of Treg cells. The combination therapy induces systemic immunomemory, effectively inhibiting contralateral tumor cell division and growth while promoting tumor rejection and preventing metastasis and recurrence. While this study primarily utilizes a subcutaneous model to demonstrate the induction of systemic immune memory, future work is necessary to validate its efficacy in preventing local recurrence and distant metastasis using orthotopic recurrence and spontaneous metastasis models. Additionally, NPs demonstrated significant antitumor efficacy in PDO models. By combining the therapeutic benefits of PDT, PTT, and immunotherapy, this work establishes a closed-loop therapeutic paradigm of "imaging navigation–inducing local multi-modal cell death–immune activation", offering an innovative strategy for solid tumor treatment that combines precise ablation with systemic immune activation. This advancement represents a critical step forward in improving therapeutic outcomes for cancer immuno-phototherapy.

CRediT authorship contribution statement

Xinyu Wang: Writing – review & editing, Writing – original draft, Formal analysis. **Yunquan Yang:** Visualization, Formal analysis, Data curation. **Shaojing Zhao:** Methodology. **Yuanyu Tang:** Methodology, Formal analysis. **E Pang:** Visualization, Formal analysis. **Wenjie Gao:** Visualization, Validation, Methodology. **Jiwei Li:** Writing – review & editing, Investigation. **Qingxu Diao:** Project administration, Methodology, Conceptualization. **Lianhong Zou:** Supervision. **Jie Zeng:** Supervision. **Minhuan Lan:** Supervision. **Jianing Yi:** Supervision, Funding acquisition.

Declaration of competing interest

The authors declare that they have no known competing financial interests or personal relationships that could have appeared to influence the work reported in this paper.

Acknowledgments

The Natural Science Foundation of Hunan Province (Nos. 2024JJ9285, 2025JJ60486); The Scientific Research Project of Hunan Provincial Department of Education (No. 22B0081); The Young Innovators Fund Program of The Affiliated Changsha Hospital of Xiangya School of Medicine (No. Y2025-15); The National Natural Science Foundation of China (No. 82500253).

Supplementary materials

Supplementary material associated with this article can be found, in the online version, at doi:10.1016/j.cclet.2025.112129.

References

[1] Y. Lu, W. Sun, J. Du, et al., JACS Au 3 (2023) 682–699.
[2] J. Zhang, W. Ma, B. Yang, et al., ACS Appl. Mater. Inter. 16 (2024) 69028–69044.

[3] H. Zhu, K. Ma, R. Ruan, et al., Chin. Chem. Lett. 35 (2024) 108536.
[4] Y. Xu, C. Li, X. Ma, et al., Proc. Natl. Acad. Sci. U. S. A. 119 (2022) e2209904119.
[5] X. Liu, Y. Lu, X. Li, et al., J. Control. Release 365 (2024) 1058–1073.
[6] Y. Ye, S. Zhao, E. Pang, et al., J. Nanobiotechnol. 23 (2025) 309.
[7] W. Li, T. Ma, T. He, et al., Chem. Eng. J. 463 (2023) 142495.
[8] Y. Cai, T. Chai, W. Nguyen, et al., Sig. Transduct. Target. Ther. 10 (2025) 115.
[9] M. Yang, L. Zhou, Y. Zhao, et al., Sci. Bull. 70 (2025) 1203–1206.
[10] S. Liu, Y. Pei, Y. Sun, et al., Aggregate 5 (2024) e547.
[11] L. Huang, S. Zhao, J. Wu, et al., Coordin. Chem. Rev. 438 (2021) 213888.
[12] L. Jia, Y. Hong, X. He, et al., Chin. Chem. Lett. 36 (2025) 109957.
[13] Z. Chen, F. Han, Y. Du, et al., Sig. Transduct. Target. Ther. 8 (2023) 70.
[14] B. Zhang, L. Lin, J. Mao, et al., Chin. Chem. Lett. 34 (2023) 108518.
[15] A.M. Shiri, T. Zhang, T. Bedke, et al., J. Hepatol. 80 (2024) 634–644.
[16] J. Yi, L. Liu, W. Gao, et al., J. Mater. Chem. B 12 (2024) 6285–6304.
[17] L. Chen, J. Huang, L. Liu, et al., Biomaterials 325 (2026) 123634.
[18] C. Huang, B. Lin, C. Chen, et al., Adv. Mater. 34 (2022) 2207593.
[19] Y. Wang, C. Wu, C. Feng, et al., Chin. Chem. Lett. 36 (2025) 109902.
[20] W. Xu, S. Wang, J. Zhang, et al., J. Nanobiotechnol. 23 (2025) 410.
[21] Y. Zhang, H. Xia, M. Yang, et al., Chin. Chem. Lett. 34 (2023) 108197.
[22] Y. Li, F. Huang, P.J. Stang, et al., ACC Chem. Res. 57 (2024) 1174–1187.
[23] Y. Tang, T. Pan, E. Pang, et al., Small 21 (2025) 2407680.
[24] B.S. Dash, Y. Lu, J. Chen, ACS Appl. Mater. Inter. 16 (2024) 13543–13562.
[25] Y. Li, Y. Li, S. Liao, et al., Chin. Chem. Lett. 36 (2025) 110832.
[26] Y. Xu, C. Li, S. Lu, et al., Nat. Commun. 13 (2022) 2009.
[27] G. Hou, Y. Chen, H. Lei, et al., Angew. Chem. Int. Ed. 64 (2025) e202419649.
[28] S. Lee, R. Karki, Y. Wang, et al., Nature 597 (2021) 415–419.